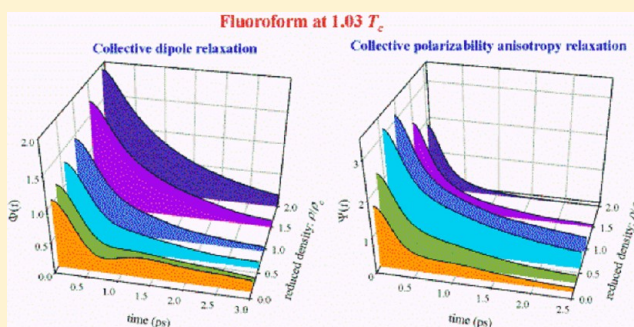


Intermolecular Structure and Collective Dynamics of Supercritical Fluoroform Studied by Molecular Dynamics Simulations

Francesca Ingrosso^{*,†,‡} and Branka M. Ladanyi^{*,§}[†]Theoretical Chemistry and Biochemistry Group SRSMC UMR 7565, CNRS – Université de Lorraine, Boulevard des Aiguillettes, BP 70239 54506 Vandoeuvre-lès-Nancy Cedex, France[‡]CNRS, SRSMC, UMR 7565, Vandoeuvre-lès-Nancy, F-54506, France[§]Department of Chemistry, Colorado State University, Fort Collins, Colorado 80523, United States

ABSTRACT: The density dependence of the local structure and of collective dynamics of a polar fluid fluoroform along an isotherm at a temperature of $1.03 T_c$ in the near-critical (NC) region, were studied by classical molecular dynamics (MD) simulations. In the case of local structure we focus on local density inhomogeneities and on orientational pair correlations that are relevant to dielectric properties and light scattering intensities. Our results show that the density dependence of the frequency shifts of fluoroform ν_2 and ν_3 modes correlates well with that of intermolecular dipole–dipole interactions. Our study of collective dynamics deals with dipole and polarizability anisotropy relaxation, experimentally accessible through far-infrared absorption, depolarized light scattering, and optical Kerr effect. Our MD simulations were performed using an all-atom nonpolarizable potential model of fluoroform. Contributions of induced dipoles to dielectric properties were included using first-order perturbation theory, and this approach was also used to include interaction-induced contributions to polarizability anisotropy relaxation. For interactions involving induced dipoles, we calculated and compared the results of a distributed polarizability model to a model with a single polarizable site located at the center-of-mass. Using a projection scheme that allows us to identify the contributions from different relaxation mechanisms, we found that dipole relaxation is dominated by collective reorientation, while in the case of polarizability anisotropy, relaxation processes related to translational dynamics make a major contribution over most of the fluid density range. The dielectric properties of fluoroform in the NC region were calculated and compared to the corresponding measurements. We found the dielectric constant and the far-infrared absorption spectrum to be in good agreement with experiments.



1. INTRODUCTION

The physical and chemical properties of supercritical fluids are used to improve the solubility of molecules and the efficiency of extraction processes and chemical reactions.^{1–3} Macroscopic density fluctuations in proximity of the critical point induce density inhomogeneities, and large changes in the system density can be easily induced by small variations in the total pressure or temperature.^{2,3} In the past two decades, the perspective of enhanced solubility and improved reactivity has motivated a vast range of applications, leading to a consistent improvement of technological and industrial processes.¹ On the other hand, the properties of such fluids are not completely understood. An increasing effort has been devoted to experimental and theoretical studies aimed at discovering more about the molecular origin of the peculiar fluid properties in the supercritical state.

Among polar supercritical fluids, fluoroform has a relatively high dipole moment⁴ (1.649 D), a critical point that is easily accessible by experiments (the critical density, temperature, and pressure are respectively $\rho_c = 0.526$ g/cm³, $T_c = 299.1$ K, and $P_c = 48$ bar),⁵ it is nontoxic, and it has a low impact on the

environment. In addition, it is available at a high level of purity at a low cost. It has often been used in experimental and theoretical studies of molecular fluid properties^{4,6–18} and solvation.^{19–29} In order to avoid macroscopic density fluctuations that occur as the critical point is approached, it is common practice to work in the so-called near-critical (NC) regime, at a temperature slightly higher than T_c . We follow this approach here by selecting $T = 1.03 T_c$ for the present study.

Our past work on fluoroform was devoted to investigating the solvent response to electronic excitation of a polar solute, coumarin 153 (C153).^{24,25} We showed that a realistic, all-atom potential for fluoroform is necessary to correctly represent the solvent rotational dynamics in the NC region.²⁵ In addition, we showed that inclusion of polarization through a perturbative approach significantly improves the agreement between the calculated and the measured solvatochromic shifts²⁴ and time-evolution of the solvation response.²⁵

Received: October 16, 2012

Revised: December 18, 2012

Published: December 21, 2012



In this work, we investigate the structure and the collective dynamics of NC fluoroform fluid at densities ranging from gas phase-like to liquid-like, using all-atom representation of the intermolecular potential.³⁰ The focus of our study of collective dynamics is on dipole and polarizability anisotropy relaxation. Both of these processes are relevant to solvent relaxation that contributes to reaction and solvation dynamics.^{31–33}

Dipole relaxation is experimentally accessible through far-infrared (far-IR) spectroscopy, while polarizability anisotropy relaxation can be measured in the frequency domain via depolarized light scattering (DLS) and in the time domain via optical Kerr effect (OKE) spectroscopy. Results of far-IR experiments³⁴ for NC fluoroform are available, while OKE data on polarizability anisotropy relaxation are available only for the liquid.⁶ Although both collective variables relax through fluctuations in molecular and interaction-induced contributions, the relative weights given to these contributions in fluoroform are quite different for dipole and polarizability anisotropy. While the molecular dipole is quite large, the molecular polarizability anisotropy is small,⁶ signaling that collective reorientation, due to the relaxation of the molecular component, will play a larger role in the case of dipole than in polarizability anisotropy dynamics. Our goal in this work is to determine the contributions of molecular and induced components to both relaxation processes as a function of fluid density, ranging from a low value of $0.13 \rho_c$ to a liquid-like value of $2.0 \rho_c$. We also investigate the dependence of the predicted response on the representation of the interaction-induced component. We compare two models for interactions involving molecular polarizability: a center–center (CC) model, based on a polarizability tensor located at the molecular center-of-mass, and a site–site (SS) model based on interacting atom-centered polarizable sites.

In our study of local structure, our focus is on local density inhomogeneities that occur in the NC regime and on intermolecular pair correlations that are relevant to understanding local orientational order that contributes to dielectric properties and DLS intensities.

This paper is organized as follows. In Section 2 we provide the theoretical framework used in the calculation of the properties of interest. In Section 3 we describe the computational procedures used in the simulations. The results are presented in Section 4. Our main findings are summarized and the paper is concluded in Section 5.

2. THEORETICAL BACKGROUND

2.1. Local Structure. In investigating the structure of NC fluoroform, we focus on measures of local density inhomogeneity, a characteristic feature of supercritical fluids,^{2,3} and on orientational pair correlations that measure local ordering associated with dipolar and quadrupolar interactions. The latter also contribute to the DLS intensity through the correlations of anisotropic polarizabilities of pairs of molecules.

Local density inhomogeneities can be quantified by analyzing the population of the coordination shell around a molecule. First of all, one can define the effective local density of the fluid based on the coordination number N_{co} at the density ρ of interest and a reference density, ρ_{ref} .^{23,24,35,36} According to this definition, the effective density is calculated with respect to ρ_{ref} :

$$\rho_{eff}(\rho) = \rho_{ref} \frac{N_{co}(\rho)}{N_{co}(\rho_{ref})} \quad (1)$$

We used as the reference the NC state corresponding to $2.0 \rho_c$ since we expect, based on previous work on NC fluoroform,^{8,15,16} that local clustering will be negligible at this liquid-like density. To calculate the coordination number, we followed two different approaches. The first one is based on evaluating the integral of the center-of-mass pair correlation function, $g^{000}(r)$, up to the position of its first minimum R_{com} :²

$$N_{co} \cong N_{com}(\rho) = 4\pi\rho \int_0^{R_{com}} dr r^2 g^{000}(r) \quad (2)$$

The second way is based on counting all the neighboring molecules that are within a distance R_{sites} from at least one of the sites in a given molecule.^{24,35} The distance R_{sites} is evaluated from SS pair correlation functions, by averaging over the SS combinations and over the density. The second way is more consistent with a nonspherical coordination shell around a polyatomic molecule. We denote the coordination number obtained in this way as N_{sites} .

Local density inhomogeneities in the NC regime are usually displayed by using two functions: one is the reduced version of eq 1, $\rho_{eff,r} = \rho_{eff}/\rho_c$ and the other is the effective reduced density increment defined as

$$\Delta\rho_{eff,r}(\rho) = \rho_{eff,r}(\rho) - \rho_r \quad (3)$$

where $\rho_r = \rho/\rho_c$ is the reduced density.

In addition to studying the local structure through $g^{000}(r)$, we also calculated several rotational-invariant projections of the intermolecular pair correlation $h(12) = h(\mathbf{r}, \Omega_1, \Omega_2)$, where \mathbf{r} is the center-of-mass distance vector and Ω_i represents the angular coordinates of molecule i . These projections are along relative orientations of molecular dipoles and quadrupoles and along the dipole–dipole potential. Thus, even though fluoroform is a nonlinear molecule, we focus on projections that include molecular orientations as a unit vector $\hat{\mathbf{u}}_i$ along the dipole of molecule i . These projections are defined as^{37,38}

$$h^{mnl}(r) = h_{00}^{mnl}(r) = \frac{\int h(12) \phi^{mnl}(\hat{\mathbf{r}}, \hat{\mathbf{u}}_1, \hat{\mathbf{u}}_2) d\Omega_1 d\Omega_2}{\int [\phi^{mnl}(\hat{\mathbf{r}}, \hat{\mathbf{u}}_1, \hat{\mathbf{u}}_2)]^2 d\Omega_1 d\Omega_2} \quad (4)$$

where $m, n, l \geq 0$ are integers with $|m - n| \leq l \leq m + n$. The CC pair distribution $g^{000}(r) = h^{000}(r) + 1$ with $\phi^{000} = 1$. The other three projections we calculate are $h^{110}(r)$, $h^{112}(r)$, and $h^{220}(r)$ for which the corresponding invariants are³⁷ $\phi^{110} = \hat{\mathbf{u}}_1 \cdot \hat{\mathbf{u}}_2$, $\phi^{112} = 3(\hat{\mathbf{u}}_1 \cdot \hat{\mathbf{r}})(\hat{\mathbf{u}}_2 \cdot \hat{\mathbf{r}}) - \hat{\mathbf{u}}_1 \cdot \hat{\mathbf{u}}_2$ and $\phi^{220} = 1 - 3(\hat{\mathbf{u}}_1 \cdot \hat{\mathbf{u}}_2)^2$. We also calculate the dipolar distance-dependent Kirkwood correlation:^{39,40}

$$G_1(r) = \langle \cos \theta(r) \rangle = h^{110}(r) / [3g^{000}(r)] \quad (5)$$

where $\cos \theta(r) = \hat{\mathbf{u}}_1 \cdot \hat{\mathbf{u}}_2$ for a pair of molecules separated by a distance r , and the symbol $\langle \dots \rangle$ denotes an equilibrium ensemble average.

2.2. Dielectric Properties. The far-infrared absorption spectrum of a fluid is related to its dielectric permittivity $\epsilon(\omega)$ by^{39,41}

$$A(\omega) = \frac{\omega \epsilon''(\omega)}{cn^2(\omega)} \quad (6)$$

where c is the speed of light in vacuum, and $n(\omega)$ is the refractive index, which can be expressed in terms of the real, $\epsilon'(\omega)$, and imaginary, $\epsilon''(\omega)$, parts of the dielectric permittivity as

$$n^2(\omega) = \frac{1}{2}[\epsilon'(\omega) + \sqrt{[\epsilon'(\omega)]^2 + [\epsilon''(\omega)]^2}] \quad (7)$$

The evaluation of the complex dielectric permittivity from simulation data is based on the calculation of the Fourier–Laplace transform $\tilde{C}(\omega)$ of the normalized collective dipole time correlation function:⁴¹

$$C(t) = \frac{\langle \mathbf{M}(0) \cdot \mathbf{M}(t) \rangle}{\langle |\mathbf{M}|^2 \rangle} \quad (8)$$

where \mathbf{M} is the collective dipole moment of the system and

$$\tilde{C}(\omega) = \int_0^\infty dt e^{i\omega t} C(t) \quad (9)$$

Real and imaginary parts of the complex dielectric permittivity are related to $\tilde{C}(\omega)$ by^{39,41}

$$\epsilon'(\omega) = \epsilon_\infty + (\epsilon_s - \epsilon_\infty)[1 - \omega \tilde{C}''(\omega)] \quad (10)$$

and

$$\epsilon''(\omega) = (\epsilon_s - \epsilon_\infty)\omega \tilde{C}'(\omega) \quad (11)$$

where $\epsilon_s = \epsilon(0)$ is the static permittivity and $\epsilon_\infty = \epsilon(\infty)$. The static permittivity is related to the mean squared dipole moment by

$$\epsilon_s = \epsilon_\infty + \frac{1}{3k_B T \epsilon_0 V} \langle |\mathbf{M}|^2 \rangle \quad (12)$$

where k_B is the Boltzmann constant, and V is the system volume.

In a polar–polarizable fluid, the total dipole \mathbf{M} includes contributions from permanent dipoles and from interactions between permanent and induced dipoles.⁴¹ In the present case, we use a nonpolarizable potential to simulate the structure and dynamics of fluoroform. However, we can include perturbatively the contributions to \mathbf{M} from interactions between permanent and induced dipoles.⁴² The dipole moment of the i th molecule may be expressed as

$$\boldsymbol{\mu}_i = \boldsymbol{\mu}_i^0 + \boldsymbol{\mu}_i^1 \quad (13)$$

where $\boldsymbol{\mu}_i^0$ is the permanent molecular dipole and

$$\boldsymbol{\mu}_i^1 = \boldsymbol{\alpha}_i \cdot \mathbf{E}_i \quad (14)$$

is the interaction-induced dipole, which depends on the molecular polarizability $\boldsymbol{\alpha}_i$ and the field \mathbf{E}_i that molecule i experiences due to the presence of other molecules. To first order, this field is due to the fixed partial charges of the other molecules:⁴²

$$\mathbf{E}_i \cong \frac{1}{4\pi\epsilon_0} \sum_{j \neq i} \sum_{p=1}^5 \frac{q_p \mathbf{r}_{ijp}}{r_{ijp}^3} \quad (15)$$

where the sum runs over all other molecules (j) and sites p (here 5 atoms) within the molecule. q_p is the partial charge of site p and \mathbf{r}_{ijp} the distance between the center of molecule i and site p of molecule j .

In eq 14 it is assumed that the molecular polarizability is located at the molecular center-of-mass, while the field is represented as arising from all the partial charge sites within the molecule. We call this interaction model the center–site (CS) model. However, for polyatomic molecules at short intermolecular separations, this model may not be accurate,⁴³ since it does not take into account the spatial extent of the

polarizability within each molecule. A way of overcoming this problem is to represent molecular polarizability as distributed over several interacting sites,^{43,44} i.e., by using an SS model. In this work, we used the site polarizability model developed by Thole⁴⁵ and modified by van Duijnen and Swart.⁴⁶ In using this model in the calculation of the interaction-induced dipole, we calculate intramolecular interactions to all orders and assume, as in eq 15, that the field at each site is due to the fixed partial charges of other molecules. In this we follow the approach developed in ref 47.

In both CS and SS models, the total collective dipole \mathbf{M} is a sum of two terms:

$$\mathbf{M} = \mathbf{M}^0 + \mathbf{M}^1 \quad (16)$$

where, for a system of N molecules,

$$\mathbf{M}^0 = \sum_{i=1}^N \boldsymbol{\mu}_i^0 \quad (17)$$

arises from molecular permanent dipoles, while \mathbf{M}^1 is a contribution from induced dipoles. In the CS model, \mathbf{M}^1 is given by

$$\mathbf{M}^1 = \mathbf{M}_{\text{CS}}^1 = \sum_{i=1}^N \boldsymbol{\mu}_i^1 \quad (18)$$

where $\boldsymbol{\mu}_i^1$ is given by eq 14. In the case of the SS model,

$$\mathbf{M}^1 = \mathbf{M}_{\text{SS}}^1 = \sum_{i=1}^N \sum_{p=1}^5 \boldsymbol{\alpha}_i^p \cdot \mathbf{E}_{ip} \quad (19)$$

where $\boldsymbol{\alpha}_i^p$ is the effective polarizability tensor^{40,47} of site p on molecule i and

$$\mathbf{E}_{ip} \cong \frac{1}{4\pi\epsilon_0} \sum_{j \neq i} \sum_{s=1}^5 \frac{q_s \mathbf{r}_{ip,js}}{r_{ip,js}^3} \quad (20)$$

is the field at the site p of molecule i due to the partial charges of other molecules.

The collective dipole time correlation is given by

$$\begin{aligned} \Phi(t) &= \frac{\langle \mathbf{M}(0) \cdot \mathbf{M}(t) \rangle}{N(\mu^0)^2} \\ &= \Phi^{00}(t) + \Phi^{01}(t) + \Phi^{11}(t) \end{aligned} \quad (21)$$

where μ^0 is the magnitude of the molecular dipole. The components of $\Phi(t)$ are the permanent dipole autocorrelation

$$\Phi^{00}(t) = \frac{\langle \mathbf{M}^0(0) \cdot \mathbf{M}^0(t) \rangle}{N(\mu^0)^2} \quad (22)$$

the interaction-induced dipole autocorrelation

$$\Phi^{11}(t) = \frac{\langle \mathbf{M}^1(0) \cdot \mathbf{M}^1(t) \rangle}{N(\mu^0)^2} \quad (23)$$

and

$$\Phi^{01}(t) = \frac{\langle \mathbf{M}^0(0) \cdot \mathbf{M}^1(t) \rangle + \langle \mathbf{M}^1(0) \cdot \mathbf{M}^0(t) \rangle}{N(\mu^0)^2} \quad (24)$$

is their cross-correlation. Note that the normalized dipole correlation $C(t)$ defined in eq 8 is related to $\Phi(t)$ by $C(t) = \Phi(t)/\Phi(0)$.

Dielectric relaxation in fluids of highly polar molecules is often dominated by the collective reorientation mechanism.^{42,47–49} In addition to \mathbf{M}^0 , a portion of \mathbf{M}^1 relaxes via this mechanism. This portion can be identified by projecting \mathbf{M}^1 along \mathbf{M}^0 ,⁴² using a scheme adopted from DLS.^{41,50} The part of $\Phi(t)$ that relaxes via collective reorientation is

$$\Phi^{\text{RR}}(t) = (1 + G)^2 \Phi^{00}(t) \quad (25)$$

where

$$G = \frac{\langle \mathbf{M}^1(0) \cdot \mathbf{M}^0(0) \rangle}{\langle |\mathbf{M}^0|^2 \rangle} = \frac{\Phi^{01}(0)}{2\Phi^{00}(0)} \quad (26)$$

is the projection and $(1 + G)^2$ acts as a local field factor,⁴¹ as a rescaling of \mathbf{M}^0 by $(1 + G)$. The remaining portion of \mathbf{M}^1

$$\Delta \mathbf{M}(t) = \mathbf{M}^1(t) - G\mathbf{M}^0(t) \quad (27)$$

is often termed “collision induced”^{42,47} and relaxes via a different mechanism, likely to be dominated by translational dynamics.

Within this projection scheme $\Phi(t)$ becomes

$$\Phi(t) = \Phi^{\text{RR}}(t) + \Phi^{\Delta\Delta}(t) + \Phi^{\text{RA}}(t) \quad (28)$$

where $\Phi^{\text{RR}}(t)$ is given by eq 25.

$$\Phi^{\Delta\Delta}(t) = \frac{\langle \Delta \mathbf{M}(0) \cdot \Delta \mathbf{M}(t) \rangle}{N(\mu^0)^2} \quad (29)$$

and

$$\Phi^{\text{RA}}(t) = \frac{(1 + G)}{N(\mu^0)^2} [\langle \Delta \mathbf{M}(0) \cdot \mathbf{M}^0(t) \rangle + \langle \Delta \mathbf{M}(t) \cdot \mathbf{M}^0(0) \rangle] \quad (30)$$

Note that the above cross term vanishes at $t = 0$: $\Phi^{\text{RA}}(0) = 0$, as can be seen from the definition of $\Delta \mathbf{M}$ (eq 27).

2.3. Polarizability Anisotropy Relaxation. The relaxation of anisotropic components of the collective polarizability tensor Π of a system of molecules is experimentally accessible in the frequency domain via DLS⁵¹ and in the time domain via time-resolved OKE.⁵²

Like the collective dipole, the polarizability is a sum of molecular and interaction-induced terms^{43,53–55}

$$\Pi = \Pi^0 + \Pi^1 \quad (31)$$

where Π^0 is a sum of polarizabilities α_i of individual molecules:

$$\Pi^0 = \sum_{i=1}^N \alpha_i \quad (32)$$

Π^1 arises from interactions between molecular induced dipoles. Taking into account these interactions to first order and assuming that molecular polarizability can be represented as located at the molecular center-of-mass, we obtain the following CC version of Π^1 :^{53,55}

$$\Pi_{\text{CC}}^1 \cong \sum_{i=1}^N \sum_{j \neq i} \alpha_i \cdot \mathbf{T}(\mathbf{r}_{ij}) \cdot \alpha_j \quad (33)$$

where \mathbf{T} is the dipole tensor:

$$\mathbf{T}(\mathbf{r}) = \frac{3\hat{\mathbf{r}}\hat{\mathbf{r}} - \mathbf{1}}{4\pi\epsilon_0 r^3} \quad (34)$$

$\hat{\mathbf{r}} = \mathbf{r}/r$ is a unit vector along \mathbf{r} , and $\mathbf{1}$ is a unit tensor.

An improved version of Π^1 is obtained by taking into account the fact that the polarizability may be distributed over several interaction sites within the molecule. Using the modified Thole model,^{45,46} as in Sec. 2.2, we obtain the SS version of Π^1 :^{40,56} In the present case, interaction sites coincide with atoms:

$$\Pi_{\text{SS}}^1 \cong \sum_{i=1}^N \sum_{j \neq i} \sum_{p=1}^5 \sum_{q=1}^5 \alpha_i^p \cdot \Upsilon(\mathbf{r}_{ip,jq}) \cdot \alpha_j^q \quad (35)$$

where Υ is the Thole-model interaction tensor,^{40,45,46} which becomes equal to \mathbf{T} at typical intermolecular distances, but is attenuated at short separations.

The time-correlation function (TCF) that represents polarizability anisotropy relaxation can be calculated from any off-diagonal element of Π ,⁵¹ for example, Π_{xz} :

$$\Psi(t) = \frac{\langle \Pi_{xz}(0) \Pi_{xz}(t) \rangle}{N\gamma^2/15} \quad (36)$$

where γ is the molecular polarizability anisotropy. For an axially symmetric molecule such as fluoroform,

$$\gamma = \alpha_{\parallel} - \alpha_{\perp} \quad (37)$$

where α_{\parallel} and α_{\perp} are, respectively, molecular polarizability components parallel and perpendicular to the molecular symmetry axis. We calculated Ψ as an average over the three off-diagonal (xy , xz , and yz) polarizability TCFs to improve the statistics.

Analogous to eq 21, the polarizability anisotropy TCF is a sum of three terms:

$$\Psi(t) = \Psi^{00}(t) + \Psi^{\text{II}}(t) + \Psi^{01}(t) \quad (38)$$

where the three component TCFs are given by

$$\Psi^{00}(t) = \frac{\langle \Pi_{xz}^0(0) \Pi_{xz}^0(t) \rangle}{N\gamma^2/15} \quad (39)$$

$$\Psi^{\text{II}}(t) = \frac{\langle \Pi_{xz}^1(0) \Pi_{xz}^1(t) \rangle}{N\gamma^2/15} \quad (40)$$

and

$$\Psi^{01}(t) = \frac{\langle \Pi_{xz}^0(0) \Pi_{xz}^1(t) \rangle + \langle \Pi_{xz}^1(0) \Pi_{xz}^0(t) \rangle}{N\gamma^2/15} \quad (41)$$

As in the case of the dipole moment, the polarizability anisotropy TCF can be cast into a projected representation,^{43,53,55} in which the portion of Π_{xz}^1 that relaxes via the same collective reorientation mechanism as Π_{xz}^0 is identified. The remainder, the “collision-induced” polarizability anisotropy is given by

$$\Delta \Pi_{xz} = \Pi_{xz}^1 - G_{xz} \Pi_{xz}^0 \quad (42)$$

where

$$G_{xz} = \frac{\langle \Pi_{xz}^0(0) \Pi_{xz}^1(0) \rangle}{\langle |\Pi_{xz}^0|^2 \rangle} = \frac{\Psi^{01}(0)}{2\Psi^{00}(0)} \quad (43)$$

$(1 + G_{xz})$ acts as a local field factor for the molecular polarizability anisotropy⁵⁷ by providing the scaling due to the local environment and identifying Π_{xz}^{R} , the part of Π_{xz} that relaxes via collective reorientation:

$$\Pi_{xz}^{\text{R}} = (1 + G_{xz}) \Pi_{xz}^0 \quad (44)$$

The total polarizability anisotropy is

$$\Pi_{xz} = \Pi_{xz}^R + \Delta\Pi_{xz} \quad (45)$$

and its TCF is

$$\Psi(t) = \Psi^{RR}(t) + \Psi^{\Delta\Delta}(t) + \Psi^{R\Delta}(t) \quad (46)$$

with the components

$$\Psi^{RR}(t) = \frac{\langle \Pi_{xz}^R(0) \Pi_{xz}^R(t) \rangle}{N\gamma^2/15} = (1 + G_{xz})^2 \Psi^{00}(t) \quad (47)$$

$$\Psi^{\Delta\Delta}(t) = \frac{\langle \Delta\Pi_{xz}(0) \Delta\Pi_{xz}(t) \rangle}{N\gamma^2/15} \quad (48)$$

and

$$\Psi^{R\Delta}(t) = \frac{\langle \Pi_{xz}^R(0) \Delta\Pi_{xz}(t) \rangle + \langle \Pi_{xz}^R(t) \Delta\Pi_{xz}(0) \rangle}{N\gamma^2/15} \quad (49)$$

As in the case of the collective dipole TCF, this projection scheme leads to initial lack of cross-correlation between rotational and collision-induced components: $\Psi^{R\Delta}(0) = 0$.

The connection between $\Psi(t)$ and OKE experiments can be obtained by calculating the nuclear response function:^{58,59}

$$R^{\text{nuc}}(t) = -\frac{\Theta(t)}{k_B T} \frac{\partial \Psi(t)}{\partial t} \quad (50)$$

where $\Theta(t)$ is the Heaviside step function.

3. COMPUTATIONAL DETAILS

Molecular dynamics (MD) simulation of all-atom model of fluoroform³⁰ at six different densities in the NC region, corresponding to the reduced density $\rho_r = \rho/\rho_c$ values 0.13, 0.3, 0.59, 0.95, 1.5, and 2.0 was performed by using DL_POLY 2.^{60,61} The critical parameters calculated for this model of fluoroform are $\rho_c = 0.630 \text{ g/cm}^3$ and $T_c = 309.0 \text{ K}$, to be compared with the experimental values $\rho_c = 0.526 \text{ g/cm}^3$ and $T_c = 299.1 \text{ K}$.⁵ After equilibration in the canonical ensemble, the production MD runs were performed in the microcanonical ensemble at the average temperature slightly higher than the critical temperature ($T = 318 \text{ K}$, corresponding to $T/T_c = 1.03$) to avoid density fluctuations on a macroscopic scale. The error bars on the simulation temperature varied from $\pm 3 \text{ K}$ at the lowest densities (0.13 and $0.3\rho_c$) to $\pm 5 \text{ K}$ at the highest densities (from 0.95 to $2.0\rho_c$), and reached $\pm 7 \text{ K}$ at $0.59\rho_c$. We used a cubic simulation box containing 256 molecules at densities below the critical density, and 500 molecules above ρ_c . The box dimensions were set to reproduce the desired density.

The original model of fluoroform³⁰ includes intramolecular bending in the interaction potential. However, in our simulations the bond lengths and angles of the fluoroform molecule were fixed at the equilibrium geometry of the model.³⁰ Fixed molecular geometry was maintained in the simulations by using the SHAKE algorithm.⁶²

The integration of the equation of motion was performed according to the Verlet leapfrog algorithm, and the long-range interactions were calculated using the Ewald method with conducting boundary conditions.⁶³ The intermolecular potential is a sum of atom–atom Coulomb + Lennard-Jones (LJ) terms. At each density, the LJ potential was cut off at half the simulation box length. We used a time step of 2 fs, and the equilibration times varied with density, from 4 ns at lower densities (up to $0.59\rho_c$) to 2 ns at the highest density, $2.0\rho_c$.

The production run lengths were of 4 ns for densities up to $0.59\rho_c$ and 3 ns for higher densities.

As can be seen from eqs 14 and 32, our calculations of dipole and polarizability anisotropy relaxation require the knowledge of the molecular polarizability tensor. The calculation of the fluoroform gas-phase molecular polarizability tensor was performed with GAUSSIAN 03.⁶⁴ Calculations were run with the Møller–Plesset method truncated at the second order (MP2),⁶⁵ with an augmented Dunning correlation-consistent basis set (aug-cc-pVDZ).⁶⁶ The geometry employed was the same as the one provided by the five-site model used in the simulation.³⁰ The values of polarizability volumes (denoted as primed quantities: $\alpha'_\perp = \alpha_\perp/(4\pi\epsilon_0)$ and $\alpha'_\parallel = \alpha_\parallel/(4\pi\epsilon_0)$) that we obtained are $\alpha'_\perp = 2.75 \text{ \AA}^3$ and $\alpha'_\parallel = 2.47 \text{ \AA}^3$. The isotropic polarizability volume, $\bar{\alpha}' = (\alpha'_\parallel + 2\alpha'_\perp)/3$ is therefore 2.67 \AA^3 , and the anisotropy $\gamma' = \alpha'_\parallel - \alpha'_\perp = -0.28 \text{ \AA}^3$. An experimental static polarizability volume $\bar{\alpha}'$ value of 3.57 \AA^3 was obtained from dielectric constant measurements,⁶⁷ from which the vibrational contribution should be subtracted, leading to a value of about 2.84 \AA^3 for the electronic polarizability. In earlier refractivity experiments⁶⁸ $\bar{\alpha}' = 2.8 \text{ \AA}^3$ was obtained. Calculations of $\bar{\alpha}'$ of CHF_3 at the SCF and CCSD levels using several different basis sets⁶⁹ are in good agreement with our results (values ranging from 2.383 \AA^3 to 2.794 \AA^3). As for the polarizability anisotropy, these calculations gave values of γ' ranging from -0.142 \AA^3 to -0.203 \AA^3 . Experimental values of the anisotropy come from the light scattering depolarization ratio^{70–72} and vary from -0.145 \AA^3 to -0.218 \AA^3 (measured at 633 nm).

As already mentioned in Section 2.2, we evaluated the effective atomic polarizability tensors by using a computational procedure described elsewhere.^{40,47,56} The values of the scalar atomic polarizabilities (in polarizability volume units) that we used as input into the modified Thole model^{45,46} are 0.449 \AA^3 , 1.355 \AA^3 , and 0.439 \AA^3 , respectively, for H, C, and F. We note that the atomic polarizability tensors calculated according to this method give the same molecular polarizability as the one evaluated through the electronic structure calculation described above.

4. RESULTS

In this section we present our results for structural and collective dynamical properties for NC fluoroform in the density range 0.13 to $2.0\rho_c$. We start with the structural properties, including measures of local clustering and orientational pair correlations, and then present our results on dielectric properties and on the collective polarizability anisotropy relaxation.

4.1. Coordination Shell and Orientational Correlations. A characteristic feature of SC fluids is local density inhomogeneity. As eq 1 shows, the effective local density ρ_{eff} depends on the enhancement, relative to a reference state, in the local coordination number. In the present case, the reference state is the NC state at $\rho_{\text{ref}} = 2.0\rho_c$. The results obtained from the definition of coordination number in eq 2 and the one based on SS correlations are displayed in Figure 1. In the case of the CC based ρ_{eff} eq 2 is integrated up to $R_{\text{com}} = 6.8 \text{ \AA}$, the average position of the first minimum of the $g^{000}(r)$ function over the values obtained at different densities. The site-based ρ_{eff} was determined by calculating the coordination number as the number of molecules that have an interaction site within a distance $R_{\text{sites}} = 4.7 \text{ \AA}$ from the center of a tagged

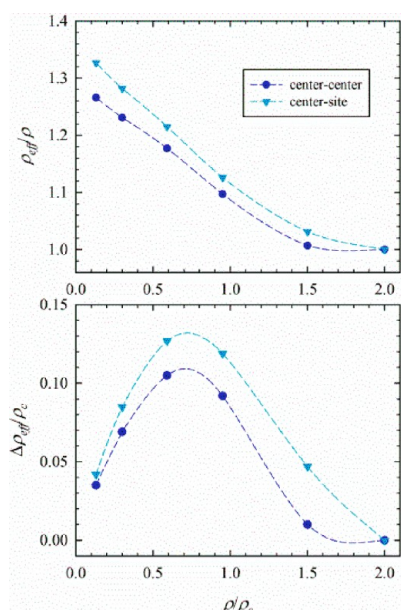


Figure 1. Effective local density (top) and local density increment (bottom) evaluated from the local coordination numbers based either on the center-of-mass (circles) or on the CS (inverted triangles) definition of the first coordination shell. The lines are drawn to guide the eye.

molecule. This distance corresponds approximately to the first minimum of center-F and center-H pair correlations.

As can be seen from Figure 1, the two sets of values of ρ_{eff} and of the local density increment, $\Delta\rho_{\text{eff}}$ are not very different, but the CS method predicts somewhat a larger amount of local density enhancement. Since fluoroform molecules have a nearly tetrahedral structure, the departure from spherical symmetry of

the coordination shell is likely to be related mainly to their charge distribution.³⁰

We explore this further by displaying in Figure 2 the results for several rotational-invariant projections, defined by eq 4, of the intermolecular pair distribution. As can be seen from the figure, the first peaks in these functions decrease in height and move to slightly lower values of r as the density increases. Structure beyond the first coordination shell becomes more prominent as ρ increases. All of the functions show a local density enhancement, which decreases with increasing ρ , consistent with the behavior of ρ_{eff}/ρ shown in Figure 1. The projections $h^{110}(r)$ and $h^{220}(r)$ are both consistent with a tendency toward parallel relative orientations of molecular dipoles, $\langle \cos \theta(r) \rangle > 0$, for molecules in the r -range of the first peak of these functions and a subsequent change in relative orientations, somewhat more evident at low densities.

The extent of intermolecular orientational correlations can be more closely related to the position-dependent Kirkwood correlation function $G_1(r)$, eq 5, displayed in Figure 3. The

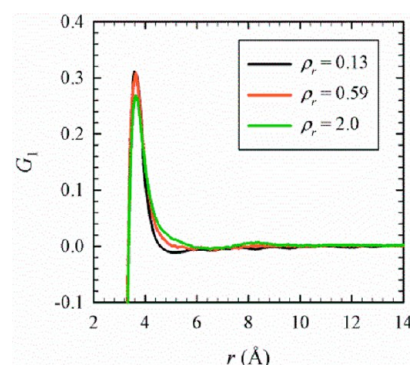


Figure 3. The position-dependent Kirkwood correlation factor $G_1(r)$ at three representative densities.

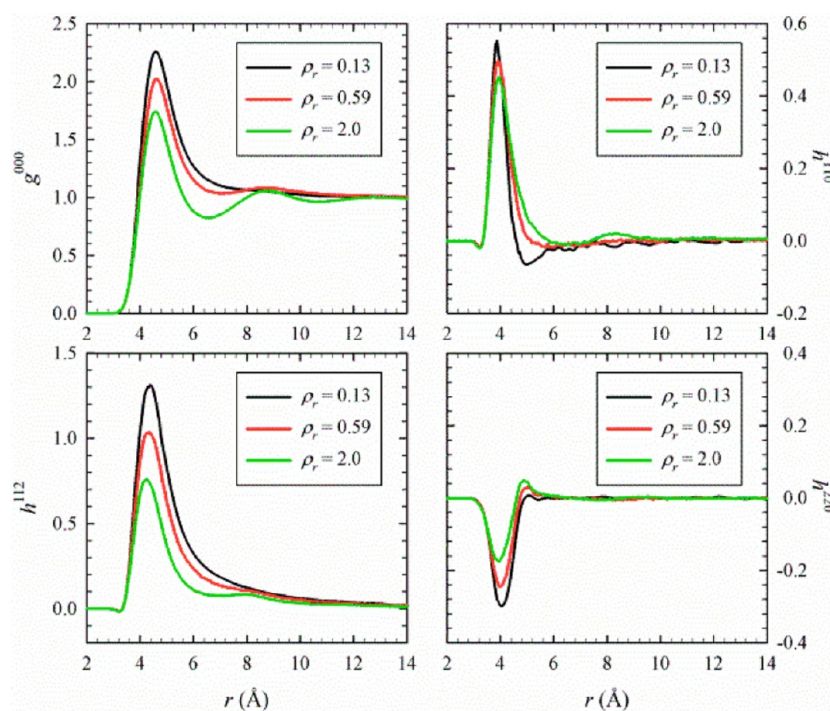


Figure 2. Rotational-invariant projections of the pair distribution function at three representative densities. Shown are g^{000} , the CC radial distribution, the dipolar and quadrupolar orientational correlations h^{110} and h^{220} , and the projection along the dipole–dipole interaction, h^{112} .

height of the first peak is related to the average relative dipolar orientation, $\langle \cos \theta(r) \rangle$ in this distance range. At the peak, the corresponding θ values increase from 72° to 74° as the density increases from 0.13 to $2.0 \rho_c$. Thus the extent of parallel alignment in the first coordination shell is fairly weak and does not depend strongly on the density.

Local density enhancement in supercritical fluoroform has been detected through frequency shifts of Raman spectra.^{15,16} The shifts in the ν_2 (symmetric C–F stretch) and ν_3 (symmetric C–F₃ deformation) were measured. The local density enhancements deduced from the shifts are different for the two modes, with the ν_2 mode showing a larger effect. By analyzing their results according to the Schweizer–Chandler theory,⁷³ Saitow et al.¹⁶ showed that most of the enhancement that they observed was due to attractive interactions. We investigate the extent of enhancement that would occur through this mechanism in our model by calculating the average dipole–dipole interaction energy⁷⁴

$$\frac{\langle U_{DD} \rangle}{N} = -\frac{4\pi}{3}(\mu^0)^2 \rho \int_0^\infty dr \frac{h^{112}(r)}{r} \quad (51)$$

Consistent with the Schweizer–Chandler theory, we assume that $\langle U_{DD} \rangle/N$ would be proportional to ρ in the absence of local density enhancement. We compare the resulting $\Delta\rho_{\text{eff}}$ to the density increments obtained from the attractive-interaction contributions to the frequency shifts $\Delta\nu_2$ and $\Delta\nu_3$, measured at the reduced temperature of 1.04.¹⁶ This comparison is displayed in Figure 4. As can be seen from the figure, all

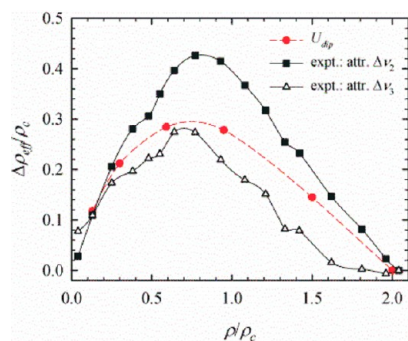


Figure 4. Local density increment obtained from $\langle U_{DD} \rangle/N$ compared to the enhancements obtained from the attractive interaction contributions to measured frequency shifts $\Delta\nu_2$ and $\Delta\nu_3$ at a temperature of 1.04 T_c .

three values of $\Delta\rho_{\text{eff}}/\rho_c$ have larger maximum values than the corresponding quantities predicted from the first solvation shell populations (Figure 1). This indicates that longer-range effects of clustering associated with $h^{112}(r)$ (Figure 2) are important in the Raman frequency shifts. We note also that the values of $\Delta\rho_{\text{eff}}/\rho_c$ as a function of density obtained from $\langle U_{DD} \rangle/N$ are intermediate between those from $\Delta\nu_2$ and $\Delta\nu_3$ and that the maxima of the three $\Delta\rho_{\text{eff}}/\rho_c$ are in the range 0.70–0.79 ρ_c with one corresponding to $\langle U_{DD} \rangle/N$ at the intermediate value of 0.76 ρ_c . Thus it appears that the density dependence of dipole–dipole interactions accounts for the major portion of the local density enhancement observed from $\Delta\nu_2$ and $\Delta\nu_3$ measurements.

4.2. Static Dielectric Properties. In Table 1 we report the density dependence of the dipolar Kirkwood correlation factor, g_1 , which is related to the degree of the orientational order between molecular dipoles. This factor was calculated as

Table 1. Static Dielectric Permittivities and Kirkwood Correlation Factors

ρ/ρ_c	ϵ_s (permanent dipoles)	ϵ_s (CS)	ϵ_s (SS)	g_1
0.13	1.178	1.161	1.159	0.991
0.30	1.421	1.469	1.457	1.034
0.59	1.873	2.049	1.999	1.052
0.95	2.600	2.909	2.769	1.079
1.5	5.013	4.624	4.218	1.169
2.0	5.328	6.484	5.692	1.295

$$g_1 = \frac{2\epsilon_s + 1}{3\epsilon_s} g_1^E \quad (52)$$

where

$$g_1^E = \frac{\langle |\mathbf{M}^0|^2 \rangle}{N(\mu^0)^2} = \Phi^{00}(0) \quad (53)$$

is the pair correlation factor appropriate for Ewald sums with conducting boundary conditions^{39,75} and ϵ_s the static dielectric constant for a nonpolarizable fluid.³⁹ It can be obtained from eq 12 by setting $\epsilon_\infty = 1$ and $\mathbf{M} = \mathbf{M}^0$.

The value of g_1 increases with density and is larger than 1 at all but the lowest density, indicating a preference for parallel orientation of the dipoles, consistent with the results displayed in Figure 2 and Figure 3. At the liquid-like density of $2.0 \rho_c$ fluoroform, g_1 is larger than that of liquid acetonitrile,³⁹ but smaller than that for protic polar liquids (water, methanol and ethanol).^{76–78}

The calculation of the static dielectric permittivity ϵ_s was performed according to eq 12. In calculating ϵ_s for the CS and SS polarizable models (eqs 18 and 19) we applied the relationship $\epsilon_\infty \cong n^2$, valid at high frequencies.⁷⁹ The refractive index n as a function of density provided in ref 22 was employed in the calculations. The results are shown in Figure 5.

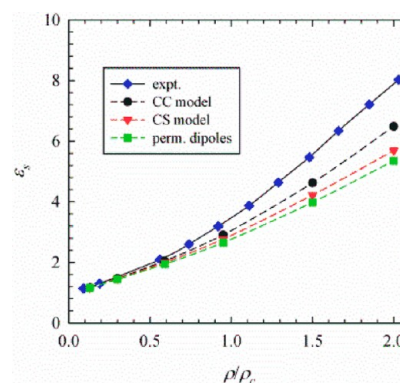


Figure 5. Static dielectric permittivity versus reduced density, ρ/ρ_c . Experimental values of ϵ_s are compared to the calculated values obtained by considering only the contributions of permanent dipoles and by also including the contributions of induced dipoles via the CS and the SS models.

As can be seen from the figures, the agreement with experiment²² is fairly good, but the calculated values of ϵ_s somewhat underestimate this quantity at higher densities. The deviation from experimental values diminishes when contributions from induced dipoles are added. Interestingly, the CS model, which is expected to be less accurate than the distributed-polarizability SS model, leads to a closer agreement

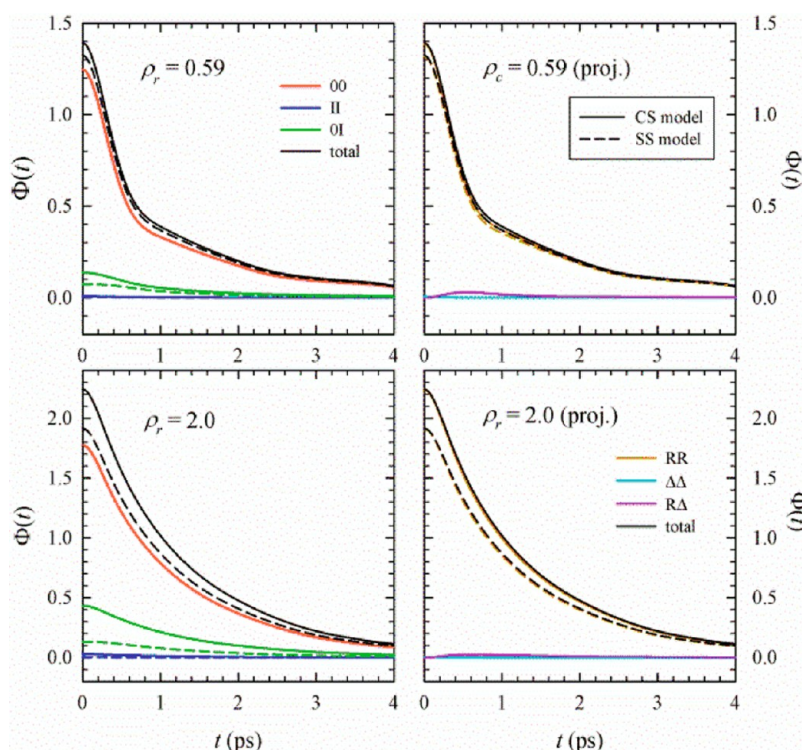


Figure 6. Components of the dipole TCF $\Phi(t)$ in the unprojected (left) and projected (right) representations. Results are shown at two reduced densities $\rho_r = 0.59$ (top) and 2.0 (bottom).

with experiment. The present results suggest that the nonpolarizable potential model that we used in our simulations may underestimate somewhat dipolar-symmetry orientational pair correlations in fluorofrom at higher densities.

4.3. Dielectric Relaxation and Far-Infrared Absorption. We analyze now the different components of the dipole TCF in the NC region. First of all, we present a comparison between the CS and SS models at two representative densities (Figure 6). In this figure, the total dipole TCF is shown along with its components in the unprojected and projected representations. The former representation is specified by eqs 21–24 and the latter by eqs 25–30. The G factors, defined in eq 26, are collected in Table 2.

Table 2. Dipolar G Factors: Projection of Induced along Permanent Dipoles

ρ_r	G (CS)	G (SS)
0.13	0.016	0.009
0.30	0.033	0.019
0.59	0.055	0.029
0.95	0.076	0.035
1.5	0.103	0.038
2.0	0.122	0.038

As can be seen from Figure 6, the effect of induced dipoles is to enhance the magnitude of $\Phi(t)$ above the value of the permanent dipole component, $\Phi^{00}(t)$. This enhancement is due mainly to the contribution of the permanent-induced cross term, $\Phi^{01}(t)$. The contribution of this term increases with increasing density, but in the case of the SS model remains quite small at all densities. Its magnitude can be gauged from the $G (= 0.5\Phi^{01}(0)/\Phi^{00}(0))$ values shown in Table 2. These indicate that the difference between the results of the two

models grows with increasing density, which is reasonable, given that the two representations of interaction-induced dipole \mathbf{M}^1 differ mainly at short-range.

The results in Figure 6 for the projected representation illustrate the fact that most of \mathbf{M}^1 projects along the permanent dipole \mathbf{M}^0 , with the result that in both interaction models, $\Phi(t)$ is nearly identical to the collective reorientation component, $\Phi^{RR}(t)$. Thus the main effect of induced dipoles is to enhance the magnitude of the permanent ones and not to add a significant relaxation channel. The CS and SS models differ mainly in the amount of enhancement of $\Phi^{RR}(t)$ relative to $\Phi^{00}(t)$. Since the relaxation rates of $\Phi(t)$ for both models are nearly identical, we display in Figure 7 only the SS model results.

As can be seen from the figure, the relaxation properties of $\Phi(t)$ vary with density. At the lowest density, $\Phi(t)$ exhibits a local minimum at around 0.8 ps and subsequently decays

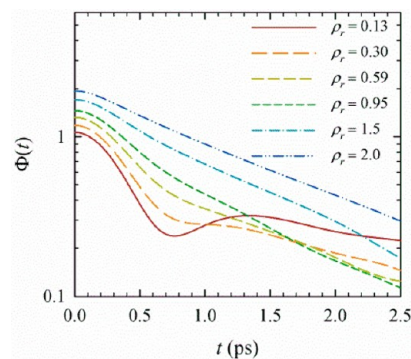


Figure 7. The total dipole TCF $\Phi(t)$ of NC fluorofrom for the SS model at six densities.

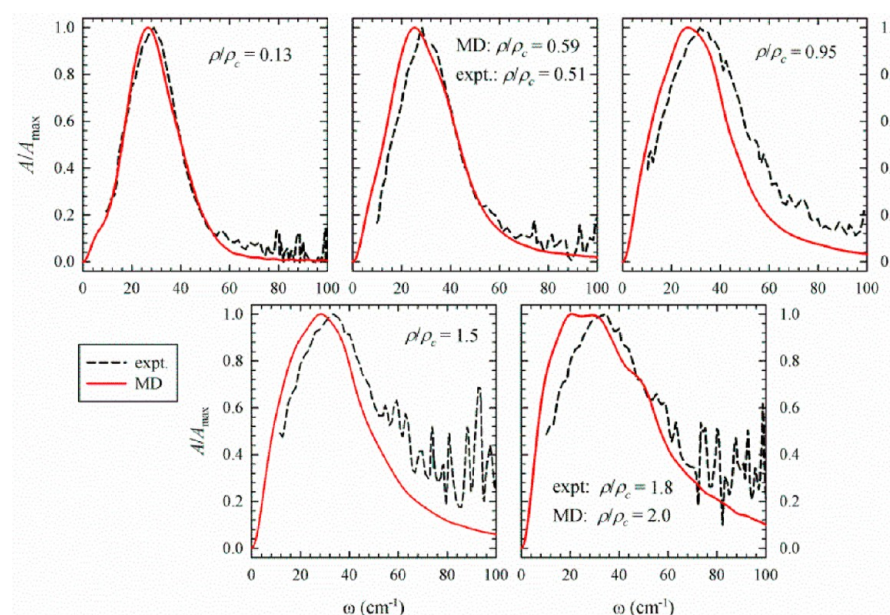


Figure 8. Comparison between calculated (MD, full line) and experimental (dashed line) normalized far-IR absorption spectra of fluoroform at the indicated densities.

slowly. This behavior is characteristic of weakly hindered rotation, which might be expected in a low density fluid.⁵¹ As rotation becomes more hindered with increasing density, the local minimum turns into an inflection point and then disappears at $\rho_r \geq 0.95$. For $\rho_r \geq 0.95$, $\Phi(t)$ behaves in a more liquid-like fashion: it exhibits initial inertial decay and subsequently decays approximately exponentially, with the decay rate decreasing with increasing density.

We present now our results for the far-IR absorption spectrum of fluoroform at different densities and compare them to experiment. The far-IR region corresponds to frequencies below those associated with intramolecular vibrations. We thus expect our potential model and representation of the collective dipole to provide a reasonable approach to the calculation of the absorption coefficient $A(\omega)$ in this frequency range.^{42,80–82} An experimental investigation³⁴ conducted at a series of densities at $T_r = 1.02$, shows that the absorption spectrum $A(\omega)$ of NC fluoroform peaks at around 30 cm^{-1} and that it shifts slightly toward higher frequencies and broadens as the density increases. The authors have interpreted their findings in terms of rotational relaxation, which becomes more hindered as the density increases. This interpretation is in accord with our findings displayed in Figure 6 and Figure 7. Comparison of our results for $A(\omega)$ (eq 6) with experiment is shown in Figure 8. In accord with the projected results shown in Figure 6, we find that $A(\omega)/A_{\text{max}}$, the normalized absorption spectrum is essentially the same for both CS and SS interaction models, i.e., the results for the two models cannot be distinguished on the scale of Figure 8. As can be seen from this figure, our results are in excellent agreement with experiment at low to moderate densities and the calculated $A(\omega)/A_{\text{max}}$ exhibits the same trends with increasing density as the experimental absorption spectrum does. However, the extent of broadening and peak shift are slightly lower than is observed experimentally. It should be noted that the experimental spectrum becomes quite noisy above $\omega \simeq 50 \text{ cm}^{-1}$ at the two highest densities, so a comparison with MD results in this frequency range becomes less clear.

4.4. Polarizability Anisotropy Relaxation. We turn now to our results for polarizability anisotropy relaxation. We start by presenting the results for the polarizability anisotropy TCF, $\Psi(t)$, followed by the results for the OKE nuclear response function, $R^{\text{nuc}}(t)$.

Figure 9 illustrates that, in contrast to dipole TCF, the polarizability anisotropy TCF is strongly influenced by interaction-induced effects. Interaction-induced portions of $\Psi(t)$ make a significant contribution to this TCF at all three densities depicted in the figure. This is a consequence of the fact, noted in Sec. 3, that CHF_3 molecules have a small polarizability anisotropy relative to the molecular isotropic polarizability, i.e., $|\gamma|/\bar{\alpha} = 0.105$. Thus the contributions of $\Psi^{\text{II}}(t)$ and $\Psi^{\text{OI}}(t)$ are non-negligible even at the lowest density displayed, $\rho_r = 0.13$. $\Psi^{\text{II}}(t)$ is the more prominent of these two at all three densities, also as a consequence of the small magnitude of $|\gamma|/\bar{\alpha}$. Among the three densities for which the results are shown in Figure 9, the relative contribution of $\Psi^{\text{II}}(t)$ is most prominent at $\rho_r = 0.59$. Its decay rate is also the slowest at this density. This seems at first to be surprising, but it is a manifestation of the partial cancellation of the positive pair and four-molecule contributions to $\Psi^{\text{II}}(t)$ by the negative three-molecule term.^{37,73,83} As the density increases, the extent of cancellation becomes larger, given that three- and four-molecule correlations become more prominent.³⁷ The extent of cancellation is greater for the longer-time portion of $\Psi^{\text{II}}(t)$ arising from mutual diffusion.³⁷ As a consequence of this, the slowest decay of $\Psi^{\text{II}}(t)$ in Figure 9 occurs at the intermediate density, $\rho_r = 0.59$.

Given that the cross term $\Psi^{\text{OI}}(t)$ is negative, the projection scheme has the effect of enhancing the “collision-induced” term $\Psi^{\Delta\Delta}(t)$ at the expense of the rotational relaxation contribution $\Psi^{\text{RR}}(t)$. As can be seen from eq 47, the decrease in intensity of $\Psi^{\text{RR}}(t)$ relative to $\Psi^{\text{OO}}(t)$ is a factor $(1 + G_{xz})^2$. The values G_{xz} , which are negative at all densities, along with time-zero values of the different contributions to the polarizability anisotropy TCF are given in Table 3.

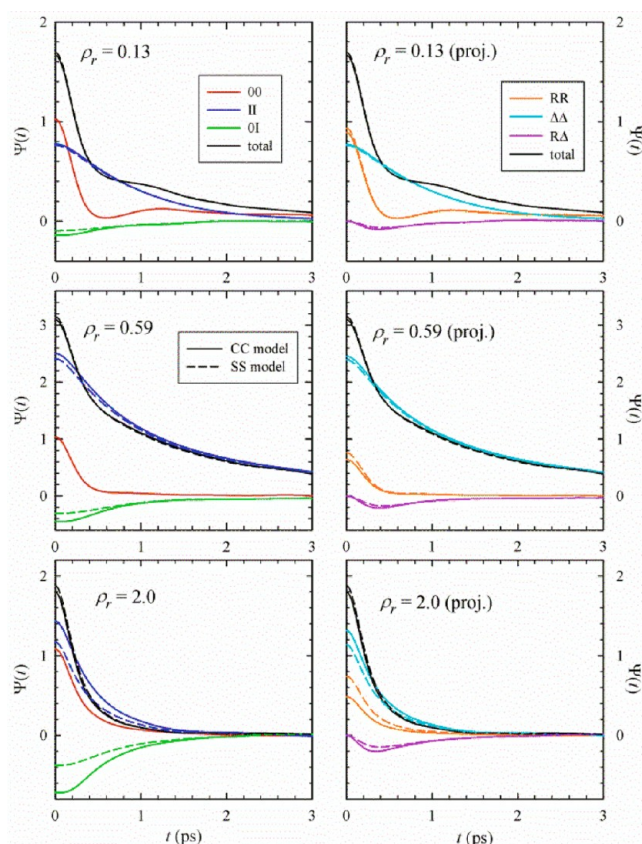


Figure 9. Polarizability TCF $\Psi(t)$ and its components in the unprojected (left) and projected (right) representations. Results for the CC (full line) and SS (dashed line) are shown at three representative densities.

A comparison of the CC and SS models for the interaction-induced contributions to $\Psi(t)$ indicates that the CC model predicts larger-magnitudes of $\Psi^{II}(t)$ and $\Psi^{0I}(t)$ than the SS model. However, given that these functions have opposite signs, the difference between the two models for the total $\Psi(t)$ is smaller than for $\Psi^{II}(t)$ and $\Psi^{0I}(t)$. Applying the projection scheme also leads to a somewhat closer agreement between the two models, given that the projected components $\Psi^{\Delta\Delta}(t)$ and $\Psi^{R\Delta}(t)$ in the SS and CC models are in closer agreement than the unprojected ones, $\Psi^{II}(t)$ and $\Psi^{0I}(t)$. At the liquid-like density of $\rho_r = 2.0$, for which the difference between the models is the largest, the present results for $\Psi(t)$ resemble the results obtained earlier for liquid chloroform by Elola and Ladanyi.⁵⁶

The contributions to the DLS intensity, i.e., to the $t = 0$ value of the polarizability anisotropy TCF are shown in Table 3. The density dependence of $\Psi(0)$ and of $\Psi^{II}(0)$ is also illustrated in the top panel of Figure 10. As can be seen from the figure, the

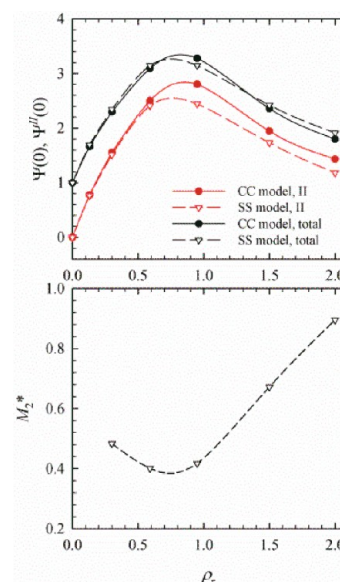


Figure 10. Top panel: Density dependence of $\Psi(0)$ and $\Psi^{II}(0)$, the initial values of the total and interaction-induced polarizability anisotropy TCFs. Bottom panel: Density dependence of the second spectral moment of the polarizability anisotropy TCF for the SS model. The lines correspond to spline fits of the data.

density dependence of $\Psi(0)$ resembles closely that of $\Psi^{II}(0)$. Both reach a maximum at $\rho_r \cong 0.8$ and then decrease, due to the cancellation effects present in $\Psi^{II}(0)$.⁸⁴ The figure also illustrates that $\Psi(0)$ is less model dependent than $\Psi^{II}(0)$. The results in Table 3 indicate that intensity of the DLS molecular component $\Psi^{00}(0)$ stays close to 1.0 at all densities and above $\rho_r = 0.13$ increases with increasing density. $\Psi^{00}(0) - 1 = \rho \langle P_2(\hat{\mathbf{u}}_1 \cdot \hat{\mathbf{u}}_2) \rangle$ is a measure of static second rank orientational pair correlations. As can be seen from Table 3, $\Psi^{00}(0) > 1$, which shows that, when averaged over intermolecular distances, the pair alignment corresponds to an angle smaller than the magic angle (54.7°). This is consistent with the behavior of $h^{220}(r)$, shown in Figure 2.

The density dependence of the reduced DLS second spectral moment, M_2^* , has often been used to measure interaction-induced effects on polarizability anisotropy dynamics.^{85–91} M_2^* is defined as⁸⁶

$$M_2^* = M_2/M_2^R \quad (54)$$

where $M_2 = -\ddot{\Psi}(0)/\Psi(0)$ is the second moment of the normalized DLS spectrum and is related to the initial curvature of $\Psi(t)/\Psi(0)$:

$$\Psi(t)/\Psi(0) = 1 - \frac{M_2}{2}t^2 + O(t^4) \quad (55)$$

Table 3. Zero-Time Values of Components of the Polarizability Anisotropy TCF

ρ_r	$\Psi^{00}(0)$	$\Psi^{II}(0)$		$\Psi^{0I}(0)$		$\Psi(0)$		G_{xz}	
		CC	SS	CC	SS	CC	SS	CC	SS
0.13	1.026	0.777	0.763	−0.139	−0.095	1.664	1.694	−0.068	−0.046
0.30	1.013	1.554	1.511	−0.272	−0.181	2.296	2.342	−0.134	−0.089
0.59	1.041	2.502	2.412	−0.448	−0.305	3.095	3.147	−0.215	−0.147
0.95	1.053	2.805	2.443	−0.599	−0.351	3.278	3.145	−0.264	−0.167
1.5	1.058	1.945	1.734	−0.645	−0.371	2.358	2.421	−0.305	−0.175
2.0	1.083	1.434	1.182	−0.717	−0.342	1.799	1.911	−0.331	−0.174

while $M_2^R = 6k_B T/I_\perp$ is the classical symmetric free rotor second spectral moment, with I_\perp being the moment of inertia perpendicular to the symmetry axis. It is also related to the initial curvature of the single-molecule orientational TCF^{92,93}

$$\langle P_2[\hat{\mathbf{u}}(0) \cdot \hat{\mathbf{u}}(t)] \rangle = 1 - \frac{M_2^R}{2} t^2 + O(t^4) \quad (56)$$

The bottom panel of Figure 10 illustrates the behavior of M_2^* for fluoroform in the SS model. The overall shape—a decrease at low densities followed by an increase at higher densities—is analogous to what has been observed for several other fluids.^{85–87,89–91} The minimum in M_2^* versus ρ_r is due predominantly to the factor of $1/\Psi(0)$. Its location correlates well with that of the $\Psi(0)$ maximum and is a measure of the relative magnitude of interaction-induced effects.⁸⁹ In the present case, these effects are quite large in view of the small $|\gamma|/\bar{\alpha}$ and resemble the results for supercritical ethane,⁹⁰ which is also characterized by a small magnitude of this ratio.

In order to illustrate more clearly, the density dependence of $\Psi(t)$ and how orientational relaxation and interaction-induced effects contribute to it, we display in Figure 11 $\Psi(t)$, $\Psi^{\Delta\Delta}(t)$, and $\Psi^{RR}(t)$ at a series of densities on the logarithmic scale. As can be seen from the figure, $\Psi^{RR}(t)$ exhibits a faster initial decay than $\Psi^{\Delta\Delta}(t)$ at all densities. At longer times it also decays faster at all but the lowest density. At $\rho_r \leq 0.30$, $\Psi^{RR}(t)$ exhibits a

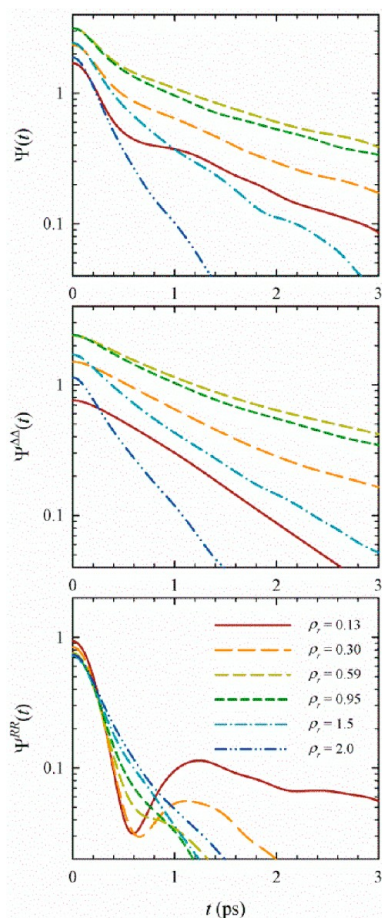


Figure 11. Log-scale representations of the polarizability anisotropy TCF $\Psi(t)$ (top panel), its collision-induced component $\Psi^{\Delta\Delta}(t)$ (middle panel), and its rotational relaxation component $\Psi^{RR}(t)$ (bottom panel), calculated using the SS model, at a series of densities.

behavior of a weakly hindered rotor,⁵¹ characterized by a local minimum at around 0.6 ps. Similar behavior was noted in Figure 7 for the dipole TCF, which is dominated by $\Phi^{RR}(t)$. However, in the DLS case, the longer-time behavior of the total TCF is at densities above $\rho_r = 0.13$ dominated by the interaction-induced component $\Psi^{\Delta\Delta}(t)$. As Figure 11 results show, due to the cancellation effects discussed earlier, the long-time decay rates of $\Psi^{\Delta\Delta}(t)$ have a rather complicated density dependence, with the slowest rate for both $\Psi^{\Delta\Delta}(t)$ and $\Psi(t)$ occurring at $\rho_r = 0.59$.

Finally, we turn to the OKE nuclear response, $R^{\text{nuc}}(t)$, eq 50. Given that this quantity is proportional to $-d\Psi/dt$, its behavior can be anticipated based on that of $\Psi(t)$. The relative contributions of orientational relaxation and interaction-induced effects are modified due to the fact that differentiation increases the weight of quickly varying processes contributing to $R^{\text{nuc}}(t)$. This is illustrated in Figure 12, where the

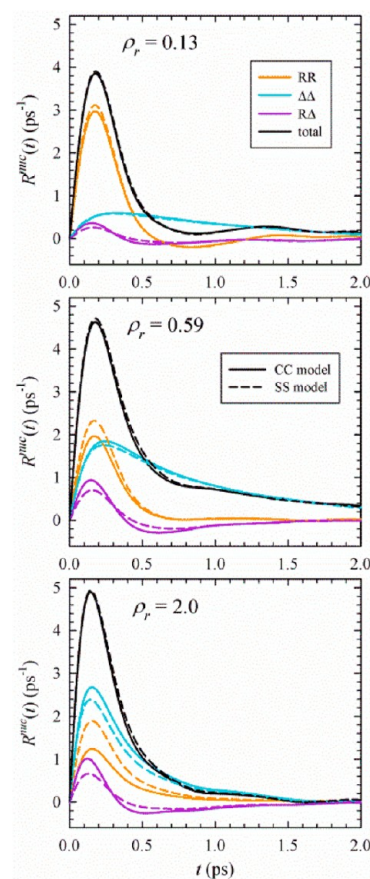


Figure 12. Contributions to the nuclear OKE response $R^{\text{nuc}}(t)$ at three representative densities in the projected representation. The factor of $1/(k_B T)$ is omitted from eq 50 in calculating $R^{\text{nuc}}(t)$.

components of $R^{\text{nuc}}(t)$ are displayed in the projected representation at the same three representative densities as in Figure 9. As can be seen from the figure, the long-time portion of $R^{\text{nuc}}(t)$ is primarily due to the collision-induced component, $R^{\Delta\Delta}(t)$, while the shorter-time portion around the peak of $R^{\text{nuc}}(t)$ has a more complicated origin. At the lowest density, the orientational relaxation component $R^{RR}(t)$ clearly dominates. At the intermediate density both $R^{RR}(t)$ and the cross-term $R^{RA}(t)$ make a significant contribution, while at the highest density all three components contribute, with the

largest contribution being due to $R^{\Delta\Delta}(t)$. This is true for both the CC and SS models.

The SS and CC models give rise to very similar $R^{\text{nuc}}(t)$. The distribution of intensity among the three components is somewhat different among the two models, with the SS model having a slightly larger $R^{\text{RR}}(t)$, mainly at the expense of $R^{\text{RD}}(t)$.

A direct comparison of the OKE nuclear responses at different densities is shown in Figure 13. The top panel displays

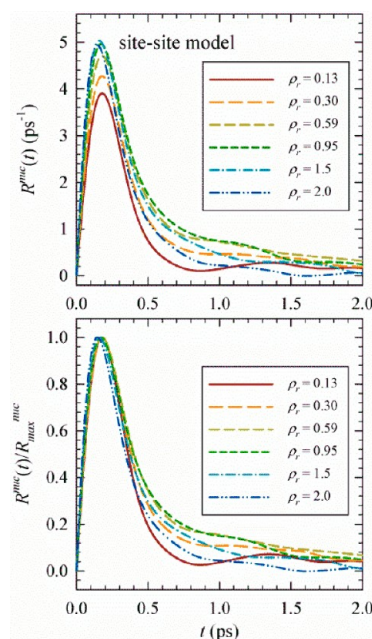


Figure 13. The nuclear OKE response in the SS model at a series of densities. The top panel depicts $R^{\text{nuc}}(t)$, and the bottom panel $R^{\text{nuc}}(t)/R^{\text{nuc}}_{\text{max}}$ the response normalized by its maximum value.

$R^{\text{nuc}}(t)$, while the bottom panel shows $R^{\text{nuc}}(t)/R^{\text{nuc}}_{\text{max}}$ the response normalized by its peak value. As can be seen from the top panel, the peak intensity increases as ρ_r increases from 0.13 to 0.95 and then levels off. The peak location changes very little with density, as can be seen more clearly from the bottom panel. The intensity of the longer-time portion of $R^{\text{nuc}}(t)$ reaches a maximum in the $\rho_r = 0.59$ to 0.95 range, likely due to the fact that the collision-induced component $R^{\Delta\Delta}(t)$ is then close to its maximum intensity. Due to the cancellation effects which increase the decay rate and diminish the intensity of this component at higher densities, the longer-time decay rate of $R^{\text{nuc}}(t)$ does not show a definite trend with respect to density.

While there are no NC fluoroform data available for comparison, OKE response for liquid fluoroform at 296 K and 125 bar has been reported.⁶ In view of the fact that these results are for a significantly lower temperature than ours, a direct comparison would not be meaningful. We can, however, use our results at densities similar to the experimental density of 1.025 g/cm³ to determine the relative contribution of rotational relaxation to the OKE response in order to make contact with the interpretation to the OKE spectral density presented by Laurent et al.⁶ In order to do this, we calculate the imaginary part of the OKE spectral density

$$\chi''(\omega) = \int_0^\infty dt \sin \omega t R^{\text{nuc}}(t) \quad (57)$$

and its RR component, $\chi''^{\text{RR}}(\omega)$, for the SS model at densities $\rho_r = 1.5$ and 2.0 , which bracket the experimental density. These results are shown in Figure 14. As can be seen from the figure,

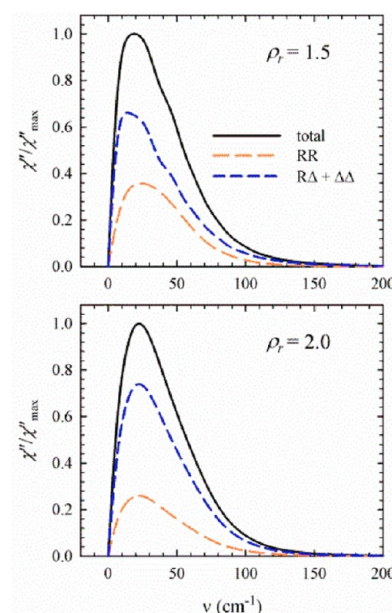


Figure 14. The OKE spectral density of NC fluoroform for the SS model, its rotational relaxation component $\chi''^{\text{RR}}(\omega)$ and the remainder $\chi''(\omega) - \chi''^{\text{RR}}(\omega) = \chi''^{\text{RD}}(\omega) + \chi''^{\Delta\Delta}(\omega)$ at two densities above ρ_c .

$\chi''^{\text{RR}}(\omega)$ remains smaller than the remaining portion of $\chi''(\omega)$ over the entire frequency range and is not the main contributor to the low-frequency peak of $\chi''(\omega)$. This is a consequence of the small molecular polarizability anisotropy of fluoroform. At both densities, the peak of the nonorientational component, $\chi''^{\text{RD}}(\omega) + \chi''^{\Delta\Delta}(\omega)$, is at a somewhat lower frequency than that of $\chi''^{\text{RR}}(\omega)$, consistent with the fact that interaction-induced components of the polarizability anisotropy TCF relax more slowly than the molecular ones at the NC temperature we considered and $\rho_r \geq 0.30$, as illustrated in Figure 11. Thus our results are not consistent with the assignment by Laurent et al.⁶ of the peak region of $\chi''(\omega)$ to orientational relaxation. We also note that the behavior of $\chi''^{\text{RR}}(\omega)$ and $\chi''^{\text{RD}}(\omega) + \chi''^{\Delta\Delta}(\omega)$ is not very different in the 0–200 cm^{−1} frequency range depicted in Figure 14, which would make it difficult to separate them through analysis of experimental data.

5. SUMMARY AND CONCLUSION

We have presented a molecular simulation study of several structural and dynamical properties of NC fluoroform along the isotherm at 1.03 T_c . We found our results to be in good agreement with the available experimental data on NC fluoroform.^{15,16,22,34} We summarize here our main findings.

Our study of intermolecular structure focused on several rotational-invariant projections of the pair distributions function as well as on several manifestations of local clustering. We showed that the effective local densities obtained from first coordination shell populations show relatively modest enhancements over the bulk densities. The considerably larger values, estimated from vibrational frequency shifts in ν_2 (C–F stretch) and ν_3 (C–F₃ deformation) modes,¹⁶ resemble the values for $\Delta\rho_{\text{eff}}$ that we obtain from the average dipole–dipole interaction, indicating that the shifts sample the effects of

clustering on intermolecular electrostatic interactions. This is reasonable in view of the fact that motion along both vibrational coordinates changes the molecular dipole.

We have investigated the dielectric properties of NC fluoroform by calculating the static dielectric constant ϵ_s , the collective dipole TCF $\Phi(t)$, and the far-IR absorption coefficient $A(\omega)$. By using a projection scheme, we have shown that the main effect of molecular induced dipoles is to enhance the magnitude of the effective collective dipole, without significantly affecting its relaxation properties. This leads to an enhancement in ϵ_s and brings it into closer agreement with experiment.²² We found that our calculated $A(\omega)$ agrees well with the experimentally determined values at a series of densities,³⁴ indicating that the fluoroform interaction model used in our work provides a reasonable representation of its collective relaxation properties in the NC region.

While the molecular permanent dipoles are relatively large, the molecular polarizability anisotropy is quite small, i.e., $|\gamma|/\bar{\alpha} = 0.105$. Thus while induced dipoles have a small effect on the relaxation rate of $\Phi(t)$, interaction-induced polarizability plays an important role in the magnitude and relaxation rate of the polarizability anisotropy TCF $\Psi(t)$. Given that the cross-correlation $\Psi^{01}(t)$ between molecular and interaction-induced polarizabilities is negative, applying the projection scheme decreases $\Psi^{RR}(t)$, the collective reorientation contribution to $\Psi(t)$ below the purely molecular component $\Psi^{00}(t)$, and enhances the collision-induced contribution $\Psi^{\Delta\Delta}(t)$. Due to partial cancellation effects between two-, three-, and four-molecule correlation contributions to $\Psi^{\Delta\Delta}(t)$, its intensity ($t = 0$ value) exhibits a maximum, and its relaxation rate a minimum at a density somewhat below ρ_c . Both of these have a strong impact on the density dependence of $\Psi(t)$, leading, among other consequences, to a pronounced maximum in the DLS intensity per molecule, $\Psi(0)$, and a deep minimum in its reduced second moment M_2^* . Over most of the density range considered, $\Psi^{RR}(t)$ dominates the short-time decay of $\Psi(t)$, while $\Psi^{\Delta\Delta}(t)$ governs its decay at longer times. Similarly, in the case of the nuclear OKE response $R^{nuc}(t)$, collective reorientation contributes mainly in the peak region, while the subsequent decay originates mostly from the collision-induced contribution.

We have used distributed and single-site polarizability representations to model interactions involving induced dipoles. The results for the two models become significantly different as the liquid-like density is approached, with the site-site model predicting somewhat smaller interaction induced effects and weaker correlations between molecular and induced moments. This result is similar to what has been observed for fluids of other symmetric rotor molecules.⁵⁶

It would be interesting to compare our results for DLS time correlations and OKE responses with experiments covering a low to liquid-like density range of NC fluoroform, and we hope that our work might inspire such studies.

AUTHOR INFORMATION

Corresponding Author

*E-mail: francesca.ingrosso@univ-lorraine.fr; Branka.Ladanyi@colostate.edu.

Notes

The authors declare no competing financial interest.

ACKNOWLEDGMENTS

This work was supported in part by the U.S. National Science Foundation Grants CHE-0911668 and CHE-1213682 to B.M.L. and by a joint Région Lorraine-Nancy Université-UMR7565 grant to F.I. Computer time by the French supercomputing center CINES is gratefully acknowledged (Project lct2550).

REFERENCES

- (1) Sunol, A. K.; Sunol, S. G. Substitution of Solvents by Safer Products and Processes. Supercritical Solvents. In *Handbook of Solvents*; Wypych, G., Ed.; ChemTec Publishing: Toronto, 2001; pp 1419–1459.
- (2) Tucker, S. C. *Chem. Rev.* **1999**, *99*, 391–418.
- (3) Kajimoto, O. *Chem. Rev.* **1999**, *99*, 355–389.
- (4) Gerschel, A.; Dimicoli, I.; Jaffre, J.; Riou, A. *Mol. Phys.* **1976**, *32*, 679–697.
- (5) Penoncello, S. G.; Shan, Z.; Jacobsen, R. T. *ASHRAE Trans.* **2000**, *106*, 739–756.
- (6) Laurent, T. F.; Hennig, H.; Ernsting, N. P.; Kovalenko, S. A. *Phys. Chem. Chem. Phys.* **2000**, *2*, 2691–2697.
- (7) Song, W.; Patel, N.; Maroncelli, M. *J. Phys. Chem. B* **2002**, *106*, 8783–8789.
- (8) Song, W.; Maroncelli, M. *Chem. Phys. Lett.* **2003**, *378*, 410–419.
- (9) Neufeind, J.; Fischer, H. E.; Schroer, W. *J. Phys.: Condens. Matter* **2000**, *12*, 8765–8776.
- (10) Mort, K. A.; Johnson, K. A.; Cooper, D. L.; Burgess, A. N.; Howells, W. S. *Mol. Phys.* **1997**, *90*, 415–424.
- (11) Hloucha, M.; Deiters, U. K. *Fluid Phase Equilib.* **1998**, *149*, 41–56.
- (12) Lang, E. W.; Prielmeier, F. X.; Radkowsitch, H.; Ludemann, H. D. *Ber. Bunsen-Ges. Phys. Chem. Chem. Phys.* **1987**, *91*, 1025–1033.
- (13) Okazaki, S.; Matsumoto, M.; Okada, I.; Maeda, K.; Kataoka, Y. *J. Chem. Phys.* **1995**, *103*, 8594–8601.
- (14) DeZwaan, J.; Hess, D. W.; Johnson, C. S. *J. Chem. Phys.* **1975**, *63*, 422–426.
- (15) Saitow, K.; Otake, K.; Nakayama, H.; Ishii, K.; Nishikawa, K. *Chem. Phys. Lett.* **2003**, *368*, 209–214.
- (16) Saitow, K.; Nakayama, H.; Ishii, K.; Nishikawa, K. *J. Phys. Chem. A* **2004**, *108*, 5770–5784.
- (17) Peng, J.; Ziegler, L. D. *J. Phys. Chem. A* **2007**, *111*, 13457–13465.
- (18) Chung, Y. H.; Li, A. H. T.; Chao, S. D. *J. Comput. Chem.* **2011**, *32*, 2414–2421.
- (19) Takahashi, K.; Fujii, K.; Sawamura, S.; Jonah, C. D. *Radiat. Phys. Chem.* **1999**, *55*, 579–581.
- (20) Kimura, Y.; Kanda, D.; Terazima, M.; Hirota, N. *J. Phys. Chem. B* **1997**, *101*, 4442.
- (21) Kimura, Y.; Iwasa, M.; Hirota, N. *Bull. Chem. Soc. Jpn.* **2001**, *74*, 1863.
- (22) Lewis, J. E.; Biswas, R.; Robinson, A. G.; Maroncelli, M. *J. Phys. Chem. B* **2001**, *105*, 3306–3318.
- (23) Biswas, R.; Lewis, J. E.; Maroncelli, M. *Chem. Phys. Lett.* **1999**, *310*, 485–494.
- (24) Ingrosso, F.; Ladanyi, B. M.; Mennucci, B.; Scalmani, G. *J. Phys. Chem. B* **2006**, *110*, 4953–4962.
- (25) Ingrosso, F.; Ladanyi, B. M. *J. Phys. Chem. B* **2006**, *110*, 10120–10129.
- (26) Kometani, N.; Arzhantsev, S.; Maroncelli, M. *J. Phys. Chem. A* **2006**, *110*, 3405–3413.
- (27) Myers, D. J.; Shigeiwa, M.; Fayer, M. D.; Cherayil, B. J. *J. Phys. Chem. B* **2000**, *104*, 2402–2414.
- (28) Myers, D. J.; Shigeiwa, M.; Cherayil, B. J.; Fayer, M. D. *J. Chem. Phys.* **2001**, *115*, 4689–4695.
- (29) Das, A.; Biswas, R.; Chakrabarti, J. *J. Phys. Chem. A* **2011**, *115*, 973–978.
- (30) Potter, S. C.; Tildesley, D. J.; Burgess, A. N.; Rogers, S. C. *Mol. Phys.* **1997**, *92*, 825–833.

- (31) Castner, E. W., Jr.; Maroncelli, M. *J. Mol. Liq.* **1998**, *77*, 1–36.
- (32) Maroncelli, M.; MacInnis, J.; Fleming, G. R. *Science* **1989**, *243*, 1674–1681.
- (33) Maroncelli, M. *J. Mol. Liq.* **1993**, *57*, 1–37.
- (34) Saitow, K.; Ohtake, H.; Sarukura, N.; Nishikawa, K. *Chem. Phys. Lett.* **2001**, *341*, 86–92.
- (35) Patel, N.; Biswas, R.; Maroncelli, M. *J. Phys. Chem. B* **2002**, *106*, 7096–7114.
- (36) Nugent, S.; Ladanyi, B. M. *J. Chem. Phys.* **2004**, *120*, 874–884.
- (37) Stell, G.; Patey, G. N.; Hoye, J. S. *Adv. Chem. Phys.* **1981**, *48*, 183–328.
- (38) Fries, P. H.; Patey, G. N. *J. Chem. Phys.* **1985**, *82*, 429–440.
- (39) Edwards, D. M. F.; Madden, P. A.; McDonald, I. R. *Mol. Phys.* **1984**, *51*, 1141–1161.
- (40) Paolantoni, M.; Ladanyi, B. M. *J. Chem. Phys.* **2002**, *117*, 3856–3873.
- (41) Madden, P.; Kivelson, D. *Adv. Chem. Phys.* **1984**, *56*, 467–566.
- (42) Edwards, D. M. F.; Madden, P. A. *Mol. Phys.* **1984**, *51*, 1163–1179.
- (43) Ladanyi, B. M. *J. Chem. Phys.* **1983**, *78*, 2189–2203.
- (44) Keyes, T.; Ladanyi, B. M. *Mol. Phys.* **1977**, *33*, 1271–1285.
- (45) Thole, B. T. *Chem. Phys.* **1981**, *59*, 341–350.
- (46) van Duijnen, P. T.; Swart, M. J. *Phys. Chem. A* **1998**, *102*, 2399–2407.
- (47) Skaf, M. S.; Fonseca, T.; Ladanyi, B. M. *J. Chem. Phys.* **1993**, *98*, 8929–8945.
- (48) Caillol, J. M.; Levesque, D.; Weis, J. J.; Perkyns, J. S.; Patey, G. N. *Mol. Phys.* **1987**, *62*, 1225–1238.
- (49) Vecchi, S. M.; Skaf, M. S. *J. Braz. Chem. Soc.* **2002**, *13*, 583–591.
- (50) Keyes, T.; Kivelson, D.; McTague, J. P. *J. Chem. Phys.* **1971**, *55*, 4096–&.
- (51) Berne, B. J.; Pecora, R. *Dynamic Light Scattering: With Applications to Chemistry, Biology, and Physics*; Wiley-Interscience: New York, 1975.
- (52) Lotshaw, W. T.; McMorro, D.; Thant, N.; Melinger, J. S.; Kitchenham, R. J. *Raman Spectrosc.* **1995**, *26*, 571–583.
- (53) Frenkel, D.; McTague, J. P. *J. Chem. Phys.* **1980**, *72*, 2801–2818.
- (54) Madden, P. A., Interaction-Induced Phenomena. In *Molecular Liquids: Dynamics and Interactions*; Barnes, A. J., Orville-Thomas, W. J., Yarwood, J., Eds.; Reidel: Dordrecht, The Netherlands, 1984; pp 431–474.
- (55) Madden, P. A.; Tildesley, D. J. *Mol. Phys.* **1985**, *55*, 969–998.
- (56) Elola, M. D.; Ladanyi, B. M. *J. Chem. Phys.* **2005**, *122*, 224506.
- (57) Keyes, T.; Ladanyi, B. M. *Adv. Chem. Phys.* **1984**, *56*, 411–465.
- (58) McMorro, D. *Opt. Commun.* **1991**, *86*, 236–244.
- (59) McMorro, D.; Lotshaw, W. T. *J. Phys. Chem.* **1991**, *95*, 10395–10406.
- (60) Smith, W.; Forester, T. R. *J. Mol. Graphics* **1996**, *14*, 136–141. Software is accessible via http://www.ccp5.ac.uk/DL_POLY_CLASSIC/.
- (61) Smith, W.; Todorov, I. T. *Mol. Simul.* **2006**, *32*, 935–943.
- (62) Ryckaert, J. P.; Ciccotti, G.; Berendsen, H. J. C. *J. Comput. Phys.* **1977**, *23*, 327–341.
- (63) Allen, M. P.; Tildesley, D. J. *Computer Simulation of Liquids*; Oxford University Press: New York, 1987.
- (64) Frisch, M. J.; Trucks, G. W.; Schlegel, H. B.; Scuseria, G. E.; Robb, M. A.; Cheeseman, J. R.; Montgomery, J., J.A.; Vreven, T.; Kudin, K. N.; Burant, J. C. et al. *Gaussian 03*, revision b.03; Gaussian, Inc.: Wallingford, CT, 2003.
- (65) Head-Gordon, M.; Pople, J. A.; Frisch, M. J. *Chem. Phys. Lett.* **1988**, *153*, 503–506.
- (66) Woon, D. E.; Dunning, T. H., Jr. *J. Chem. Phys.* **1993**, *98*, 1358–1371.
- (67) Sutter, H.; Cole, R. H. *J. Chem. Phys.* **1970**, *52*, 132–&.
- (68) Ramaswamy, K. L. *Proc. Indian Acad. Sci., Sect. A* **1935**, *2A*, 630–636.
- (69) Kobayashi, R.; Amos, R. D.; Koch, H.; Jorgensen, P. *Chem. Phys. Lett.* **1996**, *253*, 373–376.
- (70) Bridge, N. J.; Buckingham, A. D. *Proc. R. Soc. London, Ser. A* **1966**, *295*, 334–349.
- (71) Baas, F.; Van, d. H. K. D. *Physica A* **1979**, *95*, 597–601.
- (72) Miller, C. K.; Orr, B. J.; Ward, J. F. *J. Chem. Phys.* **1981**, *74*, 4858–4871.
- (73) Schweizer, K. S.; Chandler, D. *J. Chem. Phys.* **1982**, *76*, 2296–2314.
- (74) Perkyns, J. S.; Fries, P. H.; Patey, G. N. *Mol. Phys.* **1986**, *57*, 529–542.
- (75) de Leeuw, S. W.; Perram, J. W.; Smith, E. R. *Annu. Rev. Phys. Chem.* **1986**, *37*, 245–270.
- (76) Neumann, M. J. *Chem. Phys.* **1986**, *85*, 1567–1580.
- (77) Fonseca, T.; Ladanyi, B. M. *J. Chem. Phys.* **1990**, *93*, 8148–8155.
- (78) Saiz, L.; Guàrdia, E.; Padró, J. A. *J. Chem. Phys.* **2000**, *113*, 2814–2822.
- (79) Böttcher, C. J. F. *Theory of Electric Polarization: Dielectrics in Static Fields*, 2nd ed.; Elsevier: New York, 1973; Vol. 1.
- (80) Guillot, B. *J. Chem. Phys.* **1991**, *95*, 1543–1551.
- (81) Stassen, H.; Dorfmueller, T. *Chem. Phys.* **1994**, *187*, 337–348.
- (82) Beard, M. C.; Turner, G. M.; Schmittenmaer, C. A. Low Frequency, Collective Solvent Dynamics Probed with Time-Resolved THz Spectroscopy. In *Liquid Dynamics: Experiment, Simulation, and Theory*; ACS Symposium Series; American Chemical Society: Washington, DC, 2002; Vol. 820, pp 44–57.
- (83) Geiger, L. C.; Ladanyi, B. M.; Chapin, M. E. *J. Chem. Phys.* **1990**, *93*, 4533–4542.
- (84) McHale, J. L., *Molecular Spectroscopy*; Prentice Hall: Upper Saddle River, NJ, 1999.
- (85) De Santis, A.; Moretti, E.; Sampoli, M. *Mol. Phys.* **1982**, *46*, 1271–1282.
- (86) Jungwirth, P.; Winter, B. Ions at Aqueous Interfaces: From Water Surface to Hydrated Proteins. *Annu. Rev. Phys. Chem.* **2008**, *59*, 343–366.
- (87) Jungwirth, P.; Tobias, D. J. *Chem. Rev.* **2006**, *106*, 1259–1281.
- (88) Netz, R. R.; Horinek, D. *Annu. Rev. Phys. Chem.* **2012**, *63*, 401–418.
- (89) Gordon, R. G. *J. Chem. Phys.* **1965**, *43*, 1307–1312.
- (90) Versmold, H.; Zimmermann, U. *J. Chem. Soc., Faraday Trans. 2* **1987**, *83*, 1815–1824.
- (91) Zerda, T. W.; Song, X.; Jonas, J.; Ladanyi, B. M.; Geiger, L. C. *J. Chem. Phys.* **1987**, *87*, 840–851.
- (92) Lozano, N. B. H.; Stassen, H. *J. Chem. Phys.* **2009**, *130*.
- (93) Petersen, P. B.; Saykally, R. J. *Annu. Rev. Phys. Chem.* **2006**, *57*, 333–364.